Direct Measurement of the Cosmic-Ray Helium Spectrum from 40 GeV to 250 TeV with the Calorimetric Electron Telescope on the International Space Station
SUPPLEMENTAL MATERIAL

(CALET collaboration)

Supplemental material concerning "Direct Measurement of the Cosmic-Ray Helium Spectrum from 40 GeV to 250 TeV with the Calorimetric Electron Telescope on the International Space Station."

CALET HELIUM CANDIDATE

Figure S1 shows an example of helium candidate in CALET. The display is representative of a typical well reconstructed helium nucleus crossing all sub-detectors. The selected event has a shower energy of about 700 GeV in the TASC. The blue lines represent the projections of the reconstructed impinging particle trajectory in the $X - Z$ and $Y - Z$ views respectively.

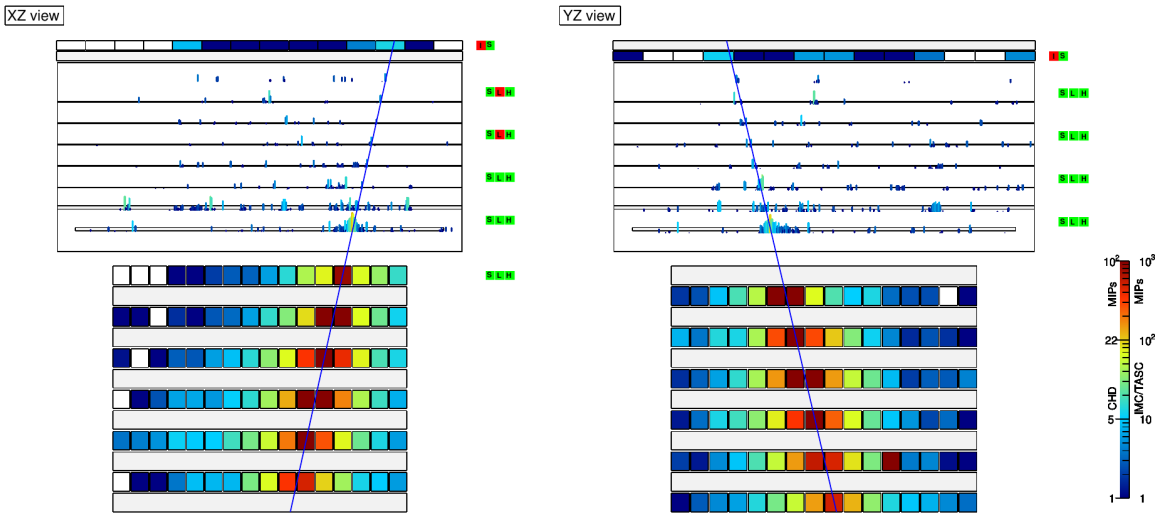

FIG. S1. Event display of a characteristic helium candidate.

CALET SELECTION EFFICIENCY

Figure S2 shows the total selection efficiency for helium nuclei (blue squares) estimated for CALET with EPICS MC simulations. In the same plot the charge selection (magenta triangles) and the HE trigger (black circles) relative efficiencies are shown, representing the two main contributions to the overall selection efficiency.

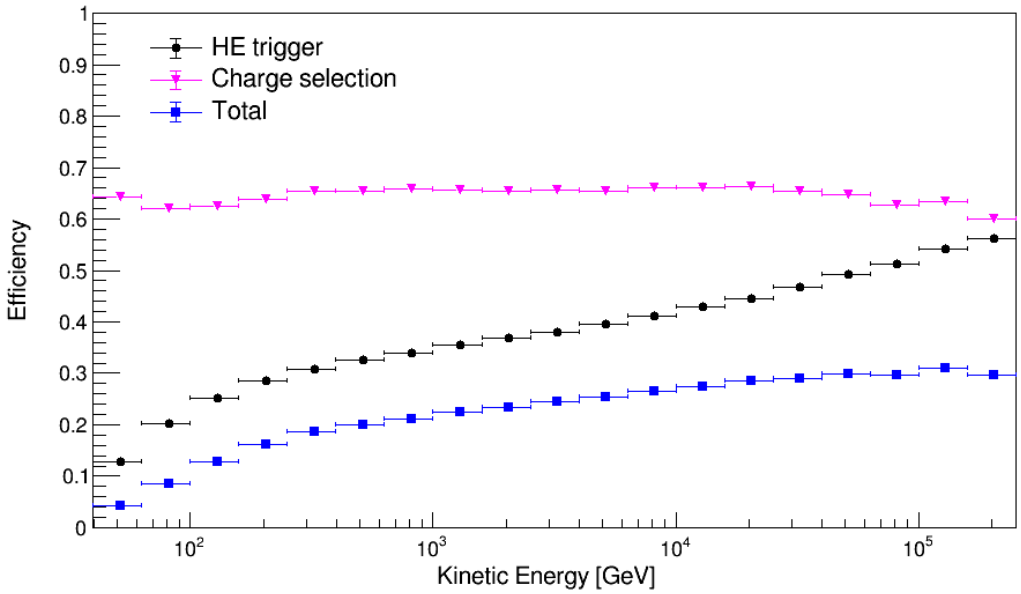

FIG. S2. The total selection efficiency for helium nuclei (blue squares) is shown together with the charge selection (magenta triangles) and the HE trigger (black circles) relative efficiencies.

CHARGE CALIBRATION AND IDENTIFICATION

Both CHD and IMC charge measurements are calibrated and corrected for their non-linear response due to the saturation of the scintillation light, and for the energy shift related to the backscattering background increasing with energy.

In order to have a perfect match between FD and MC, the MC data are fine tuned to the flight data [S1]. This additional calibration is performed fitting proton and helium charge distributions in several energy intervals (hereafter referred to as slices) with an asymmetric Landau distribution convoluted with a Gaussian (see the left panel of figure S3 for an example). Then, the FWHM and peak position of the charge distribution are computed for each energy slice, together with the Left and Right handed Half-Width-at-Half-Maximum (LWHM, RWHM), and fitted to the whole energy range with a logarithmic polynomial (dashed lines in the right panel of figure S3). The fits of the peak position and FWHM values are used, on an event by event basis, to fine tune the MC distributions. The fits to LWHM and RWHM values are used to perform an energy dependent charge cut to select the helium candidates, by applying simultaneous window cuts on the CHD and IMC reconstructed charges, requiring $3 \times \mathrm{LWHM} < Z_{CHD} < 5 \times \mathrm{RWHM}$ and $3 \times \mathrm{LWHM} < Z_{IMC} < 5 \times \mathrm{RWHM}$. An almost flat charge selection efficiency (close to 65%) is obtained, as shown in figure S2 by the magenta triangle-shaped markers.

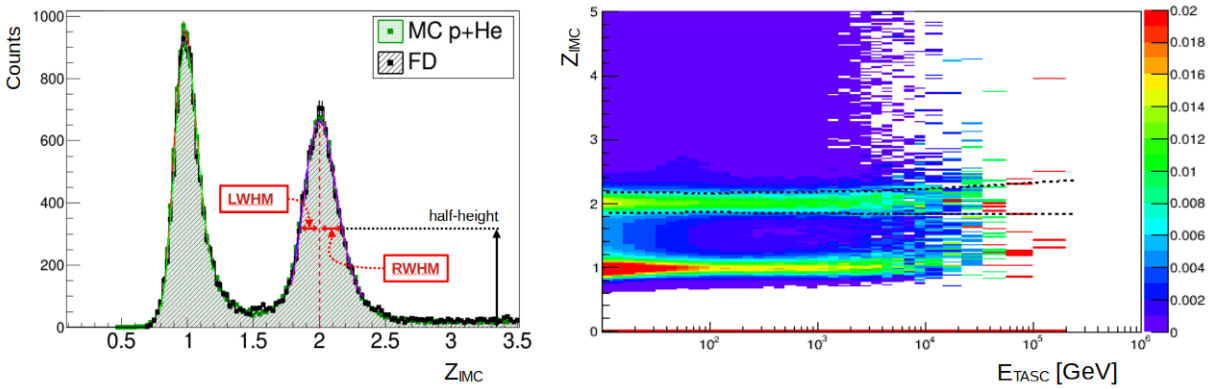

FIG. S3. Left panel: the IMC charge distribution in a given energy slice for FD (black) and the sum of proton and helium MC (green). "Lan-gauss" fit to the charge peak distribution is shown as an example, where the left and right width at half maximum of the curve are also shown. Right panel: IMC charge distribution dependence on the TASC shower energy deposit, the black dashed line shows the width of the distribution.

Energy Unfolding

In order to account for bin-to-bin migration effects due to the limited energy resolution, energy unfolding is applied to correct the E_{TASC} distribution of the selected Helium candidates and to infer the primary particle energy. In this analysis, we apply the iterative unfolding method based on the Bayes theorem [S2] implemented in the RooUnfold package [S3, S4]. Figure S4 shows the response matrix used in the unfolding procedure, which is derived using the EPICS MC simulation and applying the same selection as for FD. Each element of the matrix represents the probability that a primary helium nucleus in a given energy interval produces energy deposits in multiple bins of E_{TASC}.

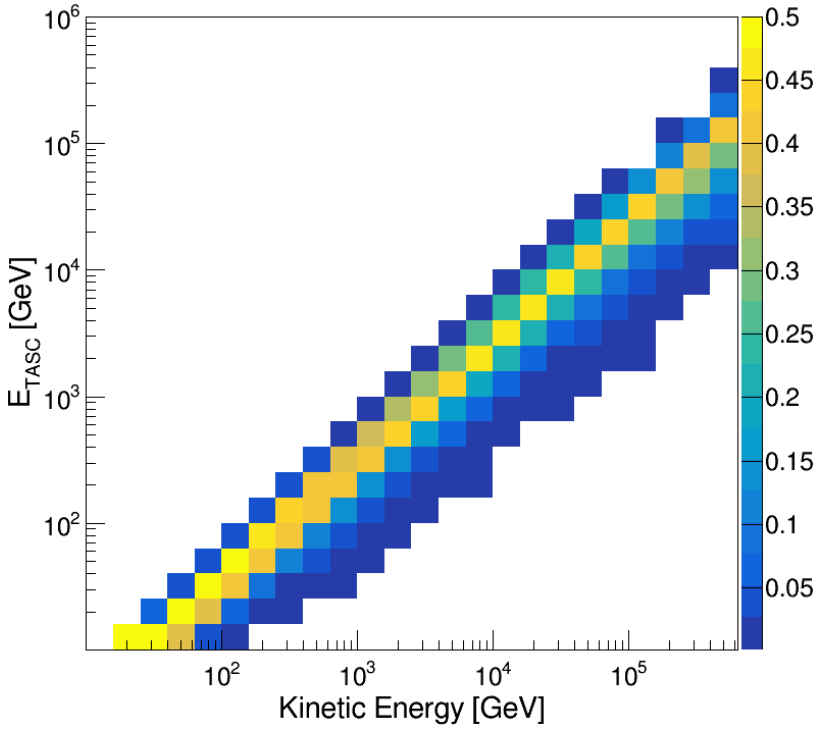

FIG. S4. Response matrix for helium, derived from MC simulations of CALET with EPICS, by applying the same selection as for FD. The color scale is associated with the probability that nuclei in a given bin of kinetic energy generate showers in different intervals of deposited energy in the TASC (E_{TASC}).

SYSTEMATIC UNCERTAINTIES

A detailed breakdown of the systematic uncertainties in the helium flux measurement is shown in figure S5, where each line and error bar represents the contribution of a different source of systematic error to the total uncertainty which is calculated as the sum in quadrature of all the known contributions and is represented by the band within the green lines in the top panel of the figure S5. On the bottom panel, the teal filled band represents the energy independent contribution of the systematic error, while all the other colored lines and bars show the individual energy dependent contributions. They include: charge identification (cyan dot-dashed lines), off-acceptance rejection cuts (black lines), geometrical acceptance and track quality cuts (magenta lines), offline trigger (azure dashed line), MC model (yellow bars), shower energy correction (blue lines), energy unfolding (gray lines) and background subtraction (dark green bars).

The systematic uncertainty of fit parameters are evaluated as follows. All the spectra used for the estimate of each source of systematic uncertainties (i.e. charge, trigger, etc.), that are obtained by varying the thresholds of the relevant cuts and the analysis parameters, are fitted with a DBPL function (Eq. 3 in the main body of the paper). Then, for each fit, the maximum difference (with either sign) between the obtained parameters and the one of the reference spectrum is taken as an estimate of the systematic error related to that source. The total uncertainty for each parameter is therefore obtained as the quadratic sum of the errors related to each systematic source. For the index change parameter ($\Delta\gamma$), the sum in quadrature of the total systematic uncertainty and the statistical error proves the $\Delta\gamma$ to be different from zero by more than 8 σ.

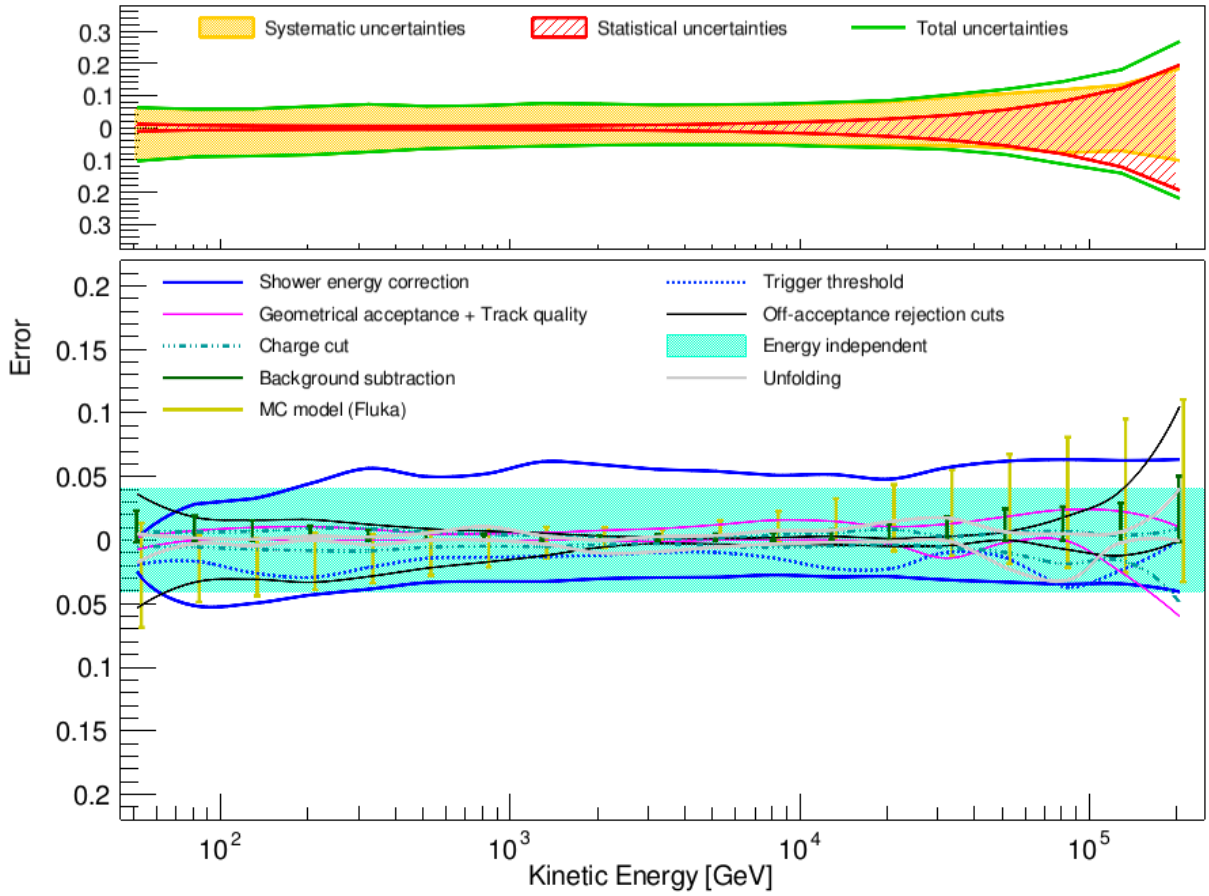

FIG. S5. Energy dependence (vs particle kinetic energy expressed in GeV) of systematic uncertainties (relative errors) for helium nuclei. On the top panel the band within the green lines shows the sum in quadrature of all the sources of systematic uncertainties. On the bottom panel the teal colored band represents the energy independent contribution of systematic error in each energy bin. All the other lines and bars show the detailed breakdown of systematic errors, stemming from charge identification, off-acceptance rejection cuts, geometrical acceptance and track quality cuts, offline trigger, MC model, shower energy correction, energy unfolding and background subtraction.

Figure S6 shows a detailed breakdown of the systematic uncertainties relative to the proton/helium flux ratio, where each line represents the contribution of a different source of systematic error to the total uncertainty, calculated as the sum in quadrature of all the contributions and represented by the band within the green lines in the top panel of the same figure. On the bottom panel, the colored lines show the individual contributions of: charge identification (magenta), off-acceptance rejection cuts (cyan), MC model (blue dashed) and energy unfolding (black dotted).

The systematic uncertainty in the p/He ratio is evaluated considering both the systematic errors of the helium flux (reported above) and of the proton flux, as reported in [S10]. For each relevant source of systematic uncertainty two different p/He ratios have been determined by calculating the fluxes at both sides of the relative error bands. The relative differences of these ratios with respect to the reference case were accounted for as systematic error. Since the proton and helium fluxes are measured with the same detector, the shower energy correction, the trigger threshold, the geometrical acceptance and the energy independent systematic are expected to give similar contributions to the two fluxes and therefore be suppressed in the ratio.

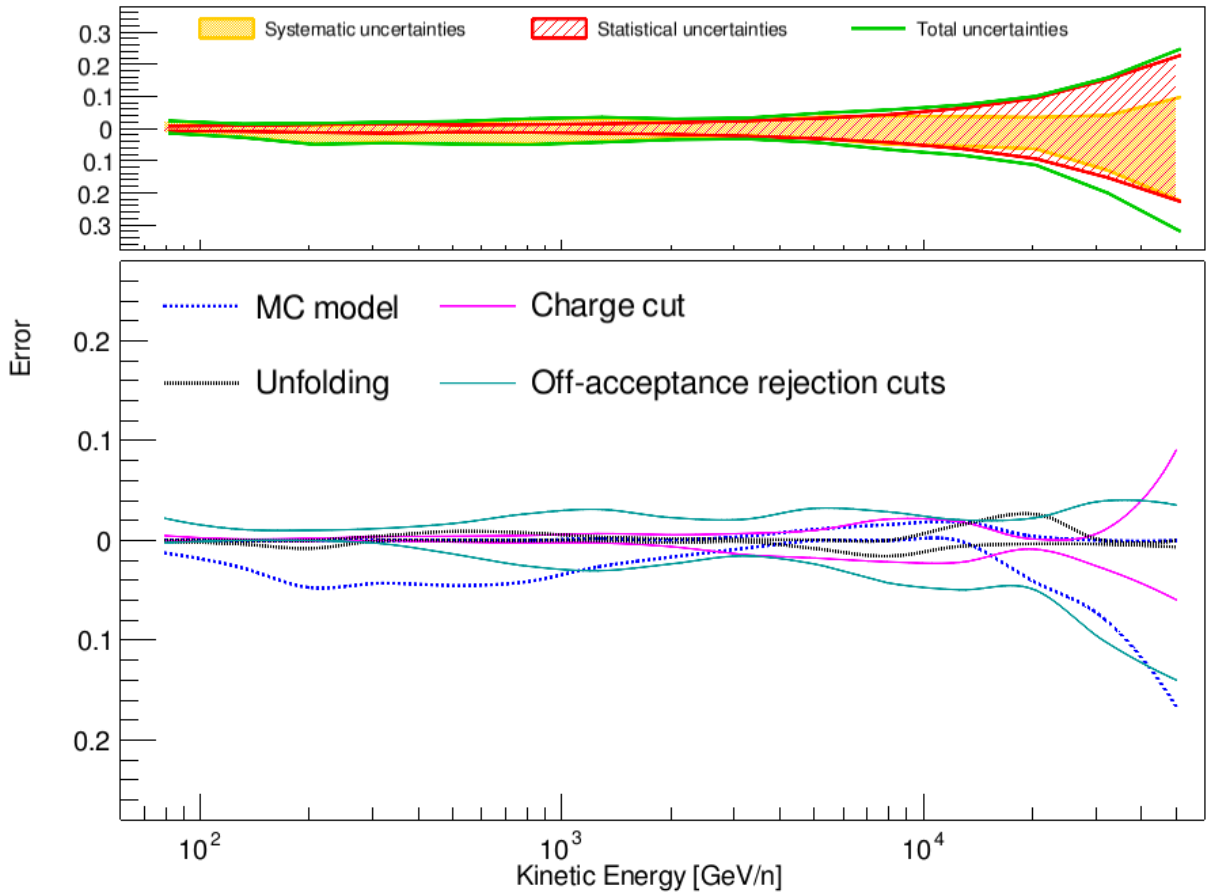

FIG. S6. Energy dependence (vs kinetic energy per nucleon expressed in GeV/n) of systematic uncertainties (relative errors) for proton/helium ratio. On the top panel the band within the green lines shows the sum in quadrature of all the sources of systematic uncertainties. On the bottom panel the lines show the detailed breakdown of systematic errors, stemming from charge identification (magenta), off-acceptance rejection cuts (cyan), MC model (blue dashed) and energy unfolding (black dotted).

RESULTS

Figure S7 shows an enlarged version of Fig. 1 in the main body of the paper, where the data from Refs [S5, S6] are added to the comparison. The energy spectrum of CR helium, as measured by CALET in an interval of kinetic energy per particle from ∼40 GeV to ∼250 TeV is presented. The red markers represent the statistical errors, while the gray band is bound by the quadratic sum of statistical and systematic errors.

The bottom panel of Fig. S8 shows the p/He flux ratio measured by CALET as a function of rigidity. The red bars represent the statistical errors and the gray band represents the quadratic sum of statistical and systematic errors. The CALET result is found to be in agreement with previous measurements from the magnetic spectrometers AMS-02 [S7] and PAMELA [S13], shown in the same plot as reference. For the sake of completeness, in the top panel of the same figure the CALET proton [S10] and helium fluxes are shown as a function of rigidity, together with previous measurements from other experiments [S11–S13].

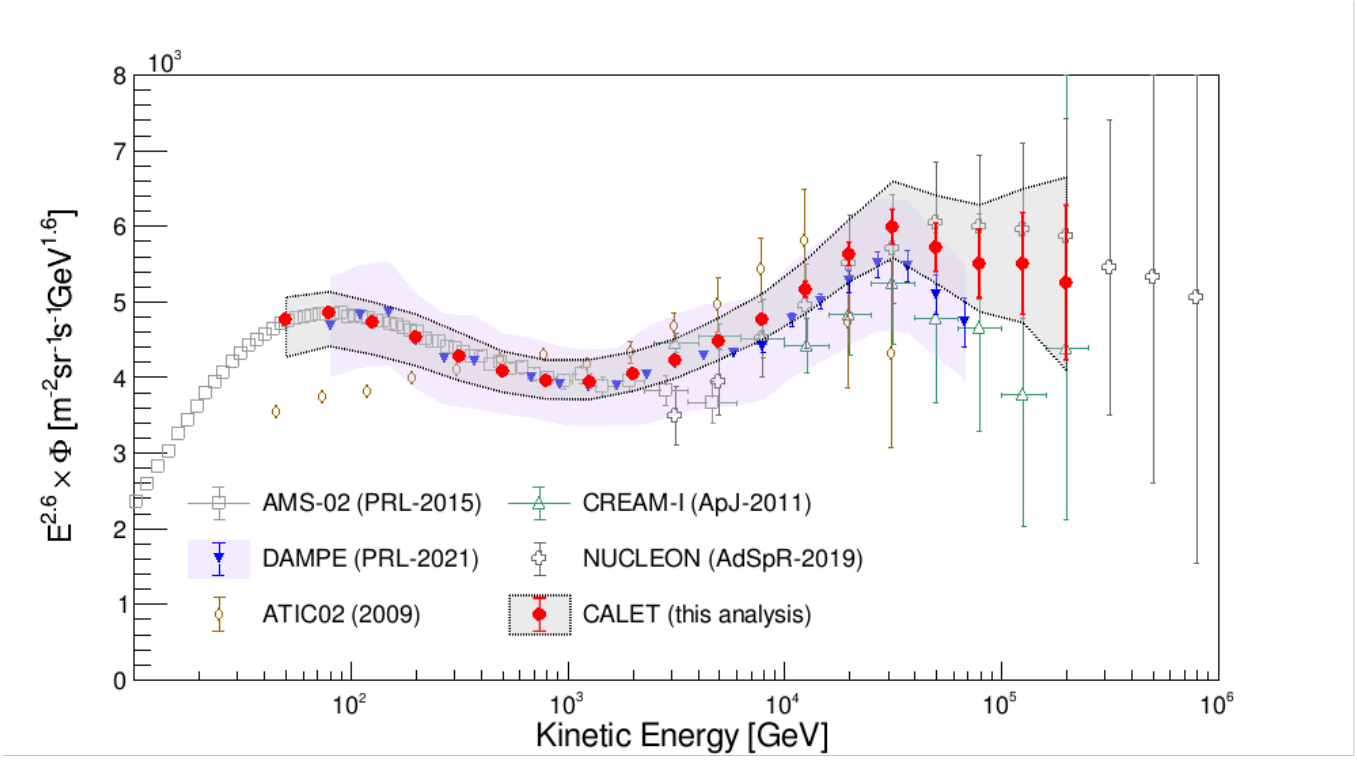

FIG. S7. Enlarged version of the cosmic-ray helium spectrum measured by CALET (red markers), compared with previous direct observations [S5–S9]. The CALET error bars refers to statistical error only, the gray band represents the quadratic sum of statistical and systematic errors. The blue bars and the light violet colored band show the statistical and systematic uncertainty for DAMPE [S8], respectively. For ATIC02 [S6] only the statistical error is represented.

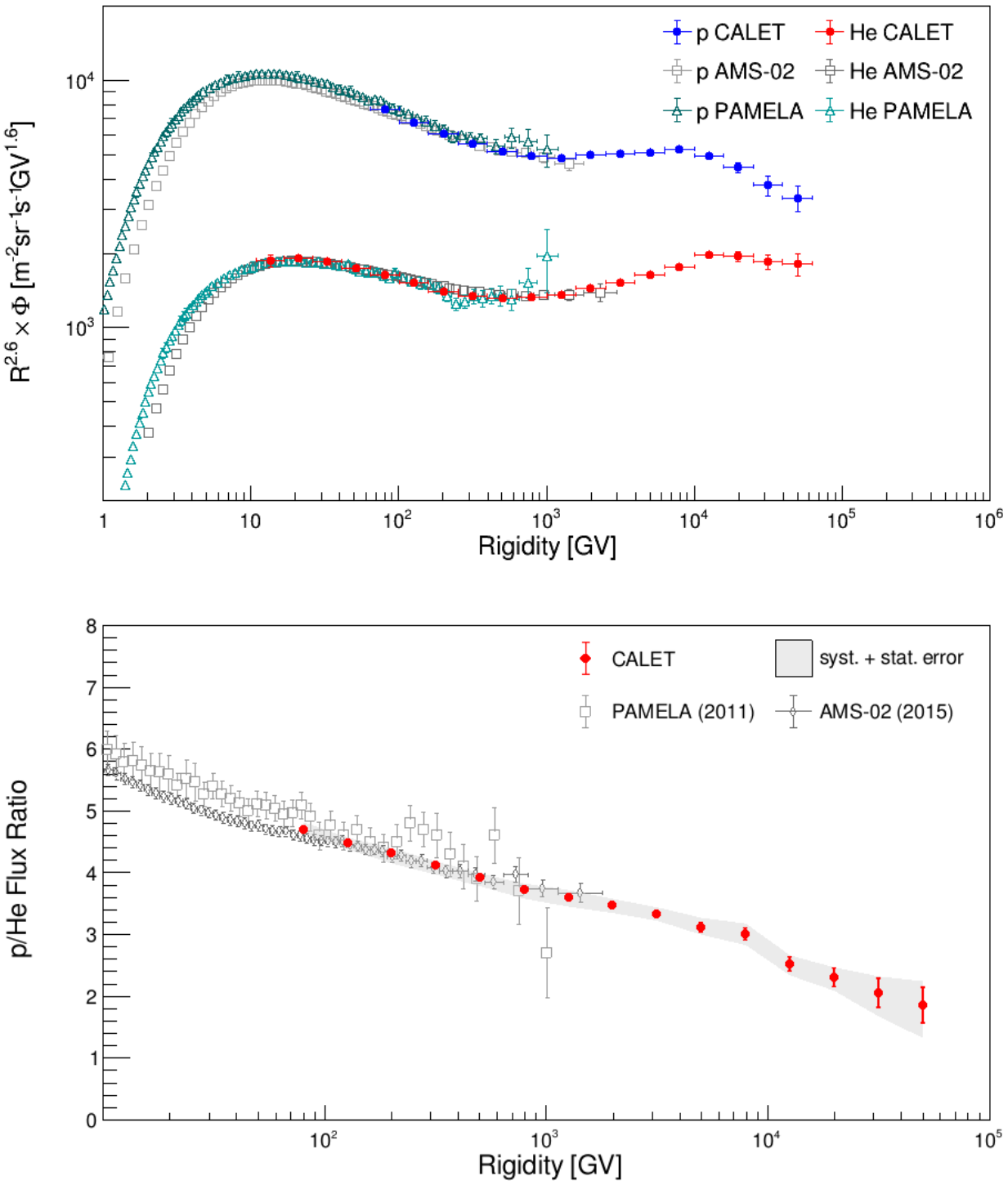

FIG. S8. The top panel shows the CALET proton [S10] and helium fluxes as a function of rigidity, together with previous measurements from other experiments [S11–S13], only the statistical errors are shown. The bottom panel shows the p/He ratio as measured by CALET as a function of rigidity, the red vertical bars represent statistical error only while the gray band represents the quadratic sum of statistical and systematic errors. Previous measurements from AMS-02 [S7] and PAMELA [S13] are shown as reference.

TABLE I. Table of CALET helium differential spectrum. The first, second and third error on the flux represents the statistical uncertainty, systematic error in normalization, and energy dependent systematic uncertainties, respectively.

Energy Bin [GeV]	Flux $[\mathrm{m}^{-2}\mathrm{sr}^{-1}\mathrm{s}^{-1}(\mathrm{GeV})^{-1}]$
39.8–63.1	$(1.812 \pm 0.020 \pm 0.074\,^{+0.084}_{-0.171}) \times 10^{-1}$
63.1–100.0	$(5.573 \pm 0.044 \pm 0.228\,^{+0.220}_{-0.448}) \times 10^{-2}$
100.0–158.5	$(1.637 \pm 0.010 \pm 0.067\,^{+0.066}_{-0.128}) \times 10^{-2}$
158.5–251.2	$(4.752 \pm 0.026 \pm 0.195\,^{+0.246}_{-0.350}) \times 10^{-3}$
251.2–398.1	$(1.354 \pm 0.007 \pm 0.056\,^{+0.081}_{-0.088}) \times 10^{-3}$
398.1–631.0	$(3.890 \pm 0.020 \pm 0.160\,^{+0.206}_{-0.199}) \times 10^{-4}$
631.0–1000.0	$(1.142 \pm 0.006 \pm 0.047\,^{+0.063}_{-0.051}) \times 10^{-4}$
1000.0–1584.9	$(3.430 \pm 0.020 \pm 0.141\,^{+0.217}_{-0.138}) \times 10^{-5}$
1584.9–2511.9	$(1.063 \pm 0.007 \pm 0.044\,^{+0.065}_{-0.038}) \times 10^{-5}$
2511.9–3981.1	$(3.352 \pm 0.030 \pm 0.137\,^{+0.192}_{-0.109}) \times 10^{-6}$
3981.1–6309.6	$(1.074 \pm 0.012 \pm 0.044\,^{+0.063}_{-0.035}) \times 10^{-6}$
6309.6–10000.0	$(3.452 \pm 0.052 \pm 0.142\,^{+0.206}_{-0.113}) \times 10^{-7}$
10000.0–15848.9	$(1.128 \pm 0.023 \pm 0.046\,^{+0.072}_{-0.043}) \times 10^{-7}$
15848.9–25118.8	$(3.714 \pm 0.102 \pm 0.152\,^{+0.256}_{-0.175}) \times 10^{-8}$
25118.8–39810.7	$(1.195 \pm 0.046 \pm 0.049\,^{+0.101}_{-0.065}) \times 10^{-8}$
39810.7–63095.6	$(3.449 \pm 0.192 \pm 0.141\,^{+0.351}_{-0.161}) \times 10^{-9}$
63095.6–100000.0	$(9.997 \pm 0.821 \pm 0.410\,^{+1.453}_{-0.667}) \times 10^{-10}$
100000.0–158489.1	$(3.025 \pm 0.369 \pm 0.124\,^{+0.478}_{-0.162}) \times 10^{-10}$
158489.1–251188.4	$(8.707 \pm 1.695 \pm 0.357\,^{+1.651}_{-0.814}) \times 10^{-11}$

TABLE II. Table of CALET proton to helium flux ratio in kinetic energy per nucleon (GeV/n). The first and second error on the ratio represents the statistical uncertainty and the systematic uncertainties, respectively.

Energy Bin [GeV/n]	Ratio
63.1–100.0	$15.5 \pm 0.1\,^{+0.4}_{-0.2}$
100.0–158.5	$14.7 \pm 0.1\,^{+0.2}_{-0.4}$
158.5–251.2	$13.7 \pm 0.2\,^{+0.1}_{-0.7}$
251.2–398.1	$12.6 \pm 0.2\,^{+0.2}_{-0.5}$
398.1–631.0	$11.5 \pm 0.1\,^{+0.2}_{-0.5}$
631.0–1000.0	$10.6 \pm 0.1\,^{+0.3}_{-0.5}$
1000.0–1584.9	$9.8 \pm 0.1\,^{+0.3}_{-0.4}$
1584.9–2511.9	$9.5 \pm 0.2\,^{+0.2}_{-0.3}$
2511.9–3981.1	$9.0 \pm 0.2\,^{+0.2}_{-0.2}$
3981.1–6309.6	$8.3 \pm 0.3\,^{+0.3}_{-0.3}$
6309.6–10000.0	$8.1 \pm 0.4\,^{+0.3}_{-0.4}$
10000.0–15848.9	$7.9 \pm 0.5\,^{+0.3}_{-0.4}$
15848.9–25118.8	$7.4 \pm 0.7\,^{+0.3}_{-0.5}$
25118.8–39810.7	$6.3 \pm 1.0\,^{+0.3}_{-0.8}$
39810.7–63095.6	$5.8 \pm 1.3\,^{+0.6}_{-1.3}$

TABLE III. Table of CALET proton to helium flux ratio in rigidity (GV). The error in the ratio refers to the statistical uncertainty only. The first and second error represents the statistical uncertainties and the systematic uncertainties, respectively.

Rigidity Bin [GV]	Ratio
64.0–100.9	$4.69 \pm 0.04^{+0.12}_{-0.04}$
100.9–159.4	$4.47 \pm 0.04^{+0.10}_{-0.08}$
159.4–252.1	$4.32 \pm 0.05^{+0.05}_{-0.16}$
252.1–399.0	$4.12 \pm 0.06^{+0.04}_{-0.13}$
399.0–631.9	$3.92 \pm 0.04^{+0.05}_{-0.13}$
631.9–1000.9	$3.72 \pm 0.04^{+0.09}_{-0.14}$
1000.9–1585.8	$3.59 \pm 0.04^{+0.12}_{-0.14}$
1585.8–2512.8	$3.47 \pm 0.05^{+0.10}_{-0.11}$
2512.8–3982.0	$3.32 \pm 0.06^{+0.10}_{-0.08}$
3982.0–6310.5	$3.12 \pm 0.08^{+0.14}_{-0.09}$
6310.5–10000.9	$3.01 \pm 0.10^{+0.14}_{-0.15}$
10000.9–15849.8	$2.52 \pm 0.11^{+0.09}_{-0.14}$
15849.8–25119.8	$2.30 \pm 0.15^{+0.08}_{-0.14}$
25119.8–39811.6	$2.04 \pm 0.24^{+0.15}_{-0.29}$
39811.6–63096.6	$1.85 \pm 0.29^{+0.28}_{-0.44}$

[S1] P. Brogi *et al.* (CALET Collaboration), in *Proceedings of Science (ICRC2021) 101* (2021).
[S2] G. D'Agostini, Nucl. Instr. and Meth. A **362**, 487 (1995).
[S3] T. Adye, in *arXiv:1105.1160v1* (2011).
[S4] R. Brun and F. Rademakers, *Nucl. Instrum. Methods Phys Res., Sect. A*, **389**, 81 (1997).
[S5] V. Grebenyuk *et al.* (NUCLEON), Adv. in Space Res. **64**, 2546 (2019).
[S6] A. Panov *et al.* (ATIC), Bull. Russian Acad. Sci. **73**, 564 (2009).
[S7] M. Aguilar *et al.* (AMS Collaboration), Phys. Rev. Lett. **115**, 211101 (2015).
[S8] F. Alemanno *et al.* (DAMPE Collaboration), Phys. Rev. Lett. **126**, 201102 (2021).
[S9] Y. Yoon *et al.*, Astrophys. J. **728**, 122 (2011).
[S10] O. Adriani *et al.* (CALET Collaboration), Phys. Rev. Lett. **129**, 101102 (2022).
[S11] M. Aguilar *et al.* (AMS Collaboration), Phys. Rev. Lett. **114**, 171103 (2015).
[S12] M. Aguilar *et al.* (AMS Collaboration), Phys. Rev. Lett. **119**, 251101 (2017).
[S13] O. Adriani *et al.*, Science **332**, 69 (2011).